A highly utilized and practical lithium-sulfur cathode enabled in all-solid-state batteries

Ashley Cronk[1], Xiaowei Wang[2]†, Jin An Sam Oh[2], So-Yeon Ham[1], Shuang Bai[1], Phillip Ridley[2], Mehdi Chouchane[4], Chen-Jui Huang[4], Diyi Cheng[2], Grayson Deysher[1], Hedi Yang[4], Baharak Sayahpour[1], Marta Vicencio[2], Choonghyeon Lee[3], Dongchan Lee[3], Min-Sang Song[3], Jihyun Jang[2]‡, Jeong Beom Lee[3*], and Ying Shirley Meng[2,4*]

[1] Materials Science and Engineering Program, University of California San Diego, La Jolla, CA, 92093, United States

[2] Department of NanoEngineering, University of California San Diego, La Jolla, CA, 92093, United States

[3] LG Energy Solution, Ltd., LG Science Park, Magokjungang 10-ro, Gangseo-gu, Seoul 07796, Korea

[4] Pritzker School of Molecular Engineering, The University of Chicago, Chicago, IL, 60637, United States

[†] Present address: Chemical Sciences and Engineering Division, Argonne National Laboratory, Argonne, Illinois, United States

[‡] Present address: Department of Chemistry, Sogang University, 35Baekbeom-ro, Mapo-gu, Seoul 04107, Republic of South Korea

*Corresponding authors. jaybilee@lgensol.com, shirleymeng@uchicago.edu

Abstract

All-solid-state batteries (ASSB) using lithium-sulfur (Li-S) cathodes, present a low-cost energy storage solution that can achieve energy densities exceeding 500 Wh kg^{-1}. However, their development in ASSBs has been hindered by poor kinetics, insulative interfaces, and (chemo)mechanical degradation, resulting in low utilization and cycle life. Here, we manipulate the meta-stability and redox activity of sulfide solid electrolytes to form ionically conductive interphases on the cathode surface using a simple and scalable synthesis approach. This creates a microstructure that enables high utilization and reversible electrochemical behavior with both sulfur and Li_2S. Bulk and morphological characterization with X-ray absorption spectroscopy quantification is used to validate reversibility. Additionally, optimizing the cathode/catholyte microstructure by tailoring particle size to the micron-scale enhances rate performance for practical operation. The coupled (chemo)mechanical behavior of Li-S cathodes and sulfide solid electrolytes was found to alleviate internal stresses with cycling, especially when paired with high capacity anodes like silicon. As a result, this approach enables high loading sulfur cathodes up to 11 mAh cm^{-2} with stable operation at room temperature. Several high energy density cell architectures are demonstrated, particularly a Li_2S anode-free pouch cell at 4.5 mAh cm^{-2} that can operate under low stack pressures. This work establishes new design strategies for Li-S cathodes, providing a pathway to enable high energy density batteries for a wide range of future applications.

Introduction

In the last decade, the need for safe and cost-effective energy storage systems has grown significantly. By 2030, the global demand for lithium-ion batteries is projected to double from 2.8 to 6 TWh[1], exceeding the projected supply. Due to the increasing adoption of electric vehicles and electrified aviation, much of this demand is driven by the transportation sector. While lithium-ion batteries using insertion-type cathodes have made substantial progress in terms of cost and energy density, these cathodes are reaching capacity and performance limitations. These limitations necessitate the development of alternatives that are safer, lightweight, with lower cost to further advance electrification technologies.[2,3] All-solid-state batteries (ASSBs) using conversion cathodes, such as lithium-sulfur (Li-S), can overcome the shortcomings of current lithium-ion battery technology. Sulfur's high specific capacity (1675 mAh g^{-1})[4] and abundance[5] make it a promising alternative energy storage solution. ASSB architecture also improves operational safety by using non-flammable solid-state electrolytes (SSE) and eliminates the polysulfide dissolution and shuttling effect, arguably the major challenge hindering the commercialization of Li-S in liquid electrolytes[6,7].

With the elimination of polysulfide dissolution in ASSBs, the primary challenge has shifted to addressing the insulating properties and slow kinetics of Li-S cathodes, in addition to their chemo-mechanical degradation from expansion and contraction[8]. The conversion from S_8 to Li_2S, results in an 79% volume change[9] – ten times greater than that of conventional cathodes. This significant volume change generates high internal pressure on the surrounding SSE matrix, leading to void formation and poor interfacial contact[10]. Consequently, most solid-state studies have adapted cathode fabrication methods from liquid systems. Typically, active materials are incorporated within high surface area carbon hosts through ball-milling[11–14], solution processes[15–17], or vapor deposition[18,19] as a means to increase conductive interfaces and constrain volume changes. Nevertheless, these methods have resulted in inconsistent utilization and cycle life. Given the large amount of carbon typically used, inadequate ionic networks and insufficient contact to sustain conversion are likely responsible. Strategies like heat treatments[20] or creating 3D solid-electrolyte structures[21] demonstrated exciting proof-of-concepts to enhance interfacial contact, but their practicality remains uncertain. Incorporating catalysts has been found to improve conversion kinetics[22,23], although using critical elements like cobalt compromises the low-cost novelty of the Li-S system. While some of these approaches have shown improvement compared to the liquid system, high areal loadings with long cycle life necessary for practicality, have yet to be demonstrated.

Li-S conversion requires "triple-phase" contact between the active materials, ionic and electronic network.[8,24] This is easier to achieve in liquid systems, as liquid electrolyte can flow through electrode pores. In ASSBs, intimate solid-solid contact can be limited and dependent on cathode architecture, including optimal particle sizes and their distribution. Ideally, a uniform distribution of active materials, SSE, and carbon should be achieved. Occasionally, this can promote decomposition or redox activity when using sulfide-based SSEs[16,25,26], formally associated with generating irreversible decomposition products at high voltages[27], especially with high surface area carbon[28]. However, the lower operating voltage of sulfur is more compatible with the lower oxidation stability of sulfide-based electrolytes, where incomplete redox may be reversible. Therefore, leveraging the redox activity of sulfide SSEs could enhance the reaction kinetics of sulfur and Li_2S. Additionally, facilitating reactions between the cathode materials and sulfide SSEs can result in beneficial interfacial properties[15,29]. To enable a practical high loading Li-S ASSBs,

new design strategies are required. Further, to maintain low-cost and make Li-S relevant for industry, the cathode design should be scalable, without relying on additives beyond the active materials, conductive agent, and SSE. This requires a deeper understanding of the potential reactivity between SSEs and Li-S cathodes, and how their coupled redox mechanisms drive electrochemical performance and chemo-mechanical behavior.

Here, we aim to develop a Li-S cathode that addresses the interfacial, kinetic, and (chemo)mechanical challenges when implemented in ASSBs, where cathode and cell level design strategies were implemented to improve utilization and cycle life (**Fig.1**). A single step mechanochemical process enabled the formation of ionically conductive interphases by facilitating bonding between the SSE and sulfur particle surface. The sulfur-SSE interphase and uniform carbon network creates a microstructure with many "triple-phase" sites for conversion. To improve cycle life, three features were enabled. First, activation of the sulfide SSE redox activity was accomplished using the single-step synthesis process and was confirmed to be reversible within the sulfur and Li_2S voltage windows. Using X-ray absorption spectroscopy (XAS), we deconvolute these capacity contributions and validate electrochemical reversibility with both sulfur and Li_2S. Second, tailoring cathode particle size to the micron scale created a cathode microstructure with reduced ionic tortuosity, enabling stable high rate cycling. Third, morphological analysis confirms that both sulfur and Li_2S cathodes undergo significant volume change. However, these volume changes were found to alleviate internal pressures, especially when paired with high-capacity anodes like silicon. As a result, unrivaled room temperature performance was demonstrated, achieving 500 cycles with 85% retention. Further, high loading sulfur cathodes up to 11 mAh cm^{-2} delivered stable cycling for over 140 cycles. A 'proof of concept' Li_2S anode-free pouch cell delivers a high reversible capacity of 900 mAh g^{-1} under practical operating conditions. This work contributes new insight on cathode and cell level design considerations, supporting the development of practical and high energy dense ASSBs using Li-S conversion chemistry.

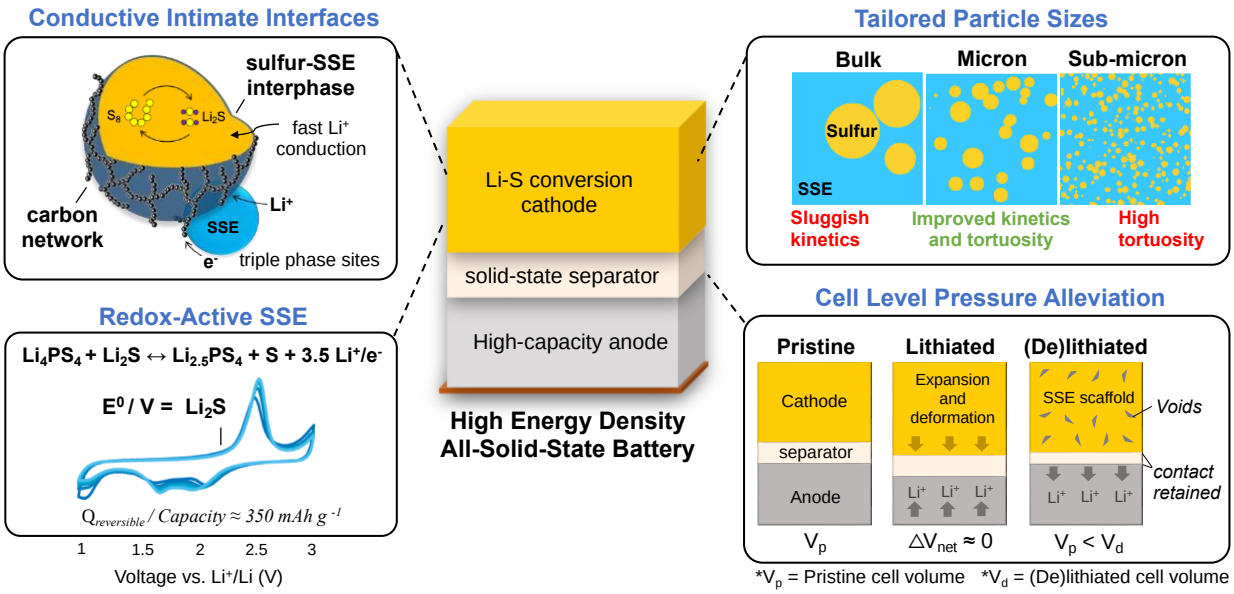

Fig. 1 | High energy density all-solid-state battery using Li-S conversion cathodes. Key features required to enable high energy density ASSBs with Li-S conversion cathodes, improving both utilization and cycle life under practical operating conditions.

Results and Discussion

Creating conductive interfaces. Cathode composite architecture including conductive interfaces are one of the critical components to enable high performing Li-S ASSBs. The potential reactivity between the active materials and the sulfide-SSE were investigated using a one-step mechanochemical milling procedure. To prove the effectiveness of this approach, two common fabrication methods were considered: hand-mixing and a multi-step milling process. Schematics illustrating each method and their expected distribution are shown in **Fig. S1,** where unmodified elemental sulfur, argyrodite Li_6PS_5Cl (LPSCl), and acetylene black (AB) carbon were used.

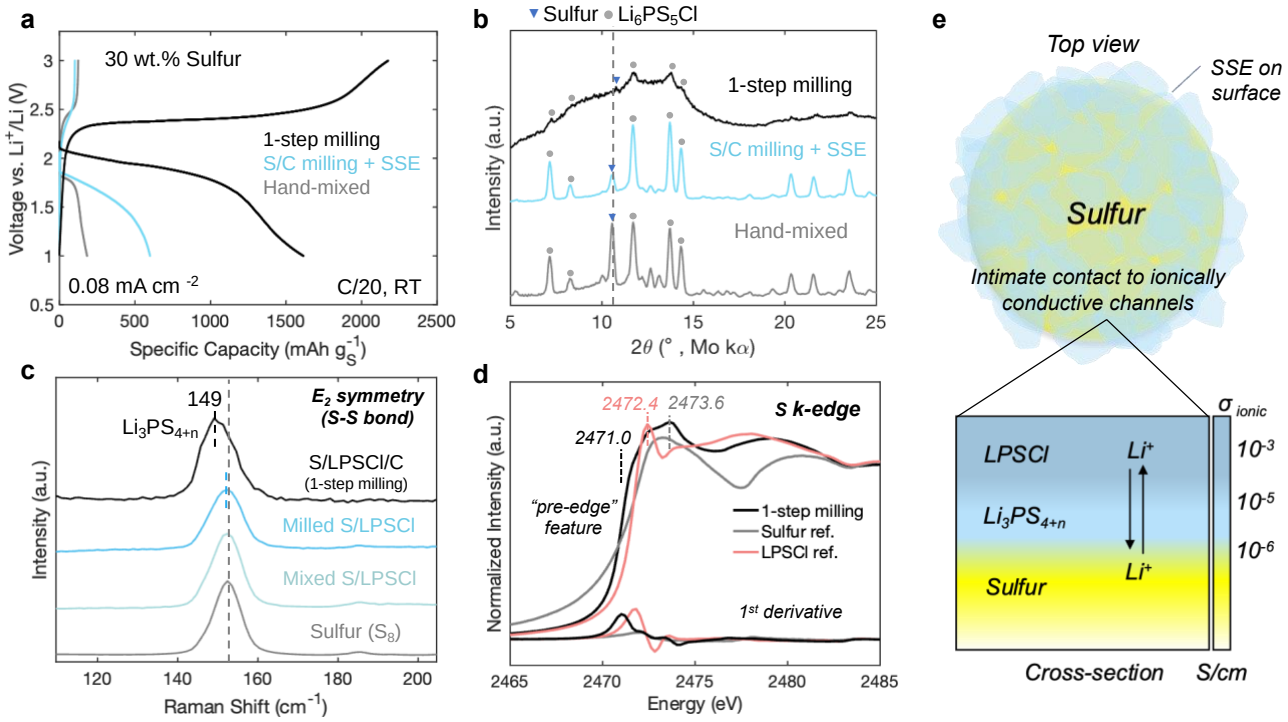

Fig. 2 | Characterizing the sulfur cathode composites after synthesis. a, Voltage profiles and (**b**) X-ray diffraction (XRD) spectra of the investigated cathode preparation methods. **c**, Raman spectroscopy and (**d**) X-ray absorption spectroscopy (XAS) of the one-step milled composite. **e**, Schematic illustrating the surface reaction with LPSCl bonded on the sulfur surface as a result of the one-step milling procedure.

Increases in sulfur utilization and discharge capacity are attained by introducing high energy milling steps to the fabrication process (**Fig. 2a)**. This is likely from improved distribution and more contact points for conversion. The multi-step process however suffered from low utilization, implying insufficient sulfur-SSE contact. It was also irreversible, marked by a low conversion efficiency (CE) of 17%. Commonly observed in prior works[13,18,25,30,31], a low CE suggests insufficient mass transport to reconvert Li_2S back to sulfur, usually requiring high activation potentials to do so[32]. The low CE can also be from the isolation of cathode particles and active surface areas after volume expansion. A comparison between hand-mixing and ball-milling has been previously investigated by Ohno *et al.*, where ball-milling achieved higher capacities, resulting in a CE of 100%.[33] However, the single-step method used here delivered a discharge

capacity near the theoretical (1615 mAh g^{-1} at 25°C) and a CE of 128%, meaning this method also activated LPSCl redox activity. A high discharge capacity coupled with SSE redox activity, suggests that this fabrication strategy produced an architecture to facilitate improved ionic/electronic transport and sufficient "triple phase" contact sites for Li-S conversion.

Figure 2b shows the diffraction patterns of the prepared composites. With all three methods, LPSCl and sulfur are detectable (**Fig. 2b**). Only the one-step method facilitated amorphization of the composite. Since the diffuse scattering of AB carbon can mask diffraction peaks, the milling procedure was done without carbon (i.e., S/LPSCl) (**fig. S2a**), where the full width at half maximum (FWHM) still increased for both characteristic peaks of sulfur and LPSCl. Amorphization, evidenced by peak broadening, can be explained from the high energy milling process, which can induce disorder.[34] The amorphization of sulfur during the fabrication process is extremely advantageous since crystalline sulfur (cyclo-S_8) requires large activation energies to break the covalent bonds between sulfur atoms[35]. Amorphous composites can lower the energy barrier for conversion and have been attributed to improved electrochemical performance[36,37]. To better understand the composite amorphization, thermogravimetric analysis (TGA) was used to quantify elemental sulfur (**fig. S3**), which should fully sublime around 350°C[38]. However, 6.5 wt.% of sulfur is unaccounted for after sweeping to 450°C, indicating alteration of the S_8 bonding environments and possible reaction with LPSCl. To investigate this, Raman spectroscopy was conducted focusing on the S-S bonding region centered at 152 cm^{-1}, which is a signature peak of E_2 symmetrical bending[39]. In this region, a redshift is observed with the milled S/LPSCl and one-step milled composites (**Fig. 2c)**. The addition of carbon further promotes this reaction. The S-S bending at lower wavelengths reveal the formation of lithium polysulfidophosphates (Li_3PS_{4+n}), where elemental sulfur bonds with the sulfur at the PS_4^{3-} terminals of LPSCl.[15,29] This observation is complimented by the reduction of the symmetric P-S stretching of the thiophosphate unit (PS_4^{3-}) in LPSCl at 425 cm^{-1} (**fig. S2b)**, suggesting that the number of sulfur atoms bonded at each terminal sulfur atom may vary. The formation of these intermediate compounds (Li_3PS_{4+n}) typically requires solvents to facilitate the reaction[15,29]. Here, we enable this interfacial reaction with a fully scalable single-step dry process. The bonding between the thiophosphate units of LPSCl and sulfur ensures intimate contact of the sulfur/SSE interface and rationalizes the high sulfur utilization shown in **Fig. 2a**.

The X-ray absorption near-edge structure (XANES) region is useful in examining oxidation states and local bonding environments. Synchrotron radiation at the Sulfur K-edge was measured for the sulfur composite and reference samples (**Fig. 2d**). Two main peaks can be observed for elemental sulfur at 2473.6 eV and LPSCl at 2472.4 eV. A "pre-edge" feature at 2470.1 eV is also evident from 1st derivatives of the spectra. "Pre-edge" features indicate a reduction of the sulfur oxidation state and have been observed for long chain polysulfides (Li_2S_y)[40]. The "pre-edge" observed here is likely from long chains of sulfur in Li_3PS_{4+n}. Ionic conductivity of the S/LPSCl composites after various milling durations were also measured, where an increase is observed after 1 hour and saturates near 2×10^{-5} S cm^{-1} with continued milling (**fig. S2c**). The increase in ionic conductivity confirms the formation of an ionically conductive phase using the mechanochemical process. However, particle morphology and chemical composition of this phase is elusive using conventional scanning electron microscopy (SEM). Therefore, low-dose cryo-TEM, high-angle annular dark-field scanning transmission electron microscopy (HAADF-STEM) imaging, and elemental mapping was conducted on multiple particles (**fig. S4 and S5**). Line scan results reveal the particle is sulfur with LPSCl on the surface (**table *S1***). These results corroborate

the interfacial reaction between sulfur and LPSCl, creating an ionically conductive phase on the sulfur particle surface. The tailored interface lowers the energy barrier for lithiation, facilitating fast lithium transport from the SSE matrix into the sulfur bulk as illustrated in **Fig. 2e**.

The interaction between LPSCl and Li_2S was also investigated. A comparison between cathode preparation methods was conducted, where comparable trends seen with sulfur is observed with Li_2S (**Fig. S6**). Hand-mixing the composite fails to cycle, and the multi-step process delivers low utilization coupled with large polarization. The one-step method, however, delivers a high specific capacity of 723 mAh g^{-1} with a high coulombic efficiency of 99.3%, indicating good reversibility. With the Li_2S cathode, the synthesis method resulted in the decomposition and amorphization of LPSCl, evidenced by undetectable peaks in the diffraction pattern and a shift of P-S stretching in PS_4^{3-} from 425 cm $^{-1}$ to 418 cm $^{-1}$, assigned to Li_3PS_4 (LPS)[41] (**fig. S7**). These results suggest that Li_2S reduced LPSCl to LPS. Despite this decomposition, the Li_2S cell exhibits stable cycling, where additional plateaus present in the voltage profile after the 1st cycle (**fig. S8**) indicating that this approach also activated redox activity from the SSE decomposition products and is electrochemically reversible.

Evaluating LPSCl redox activity and electrochemical reversibility. The redox activity of sulfide SSEs has been responsible for delivering capacity beyond the theoretical when paired with Li-S cathodes[15,16,19] and associated with irreversible electrochemical behavior[42]. Often overlooked in literature, deconvoluting the capacity contribution between sulfur and SSE is essential in accurately quantifying utilization and effectiveness of the cathode architecture. To isolate this capacity contribution and study its potential reversibility, cells with just LPSCl and carbon were evaluated.

LPSCl, like many sulfides, exhibit a narrow stability window, reducing at 1.3 V and oxidizing at 2.3 V vs. Li/Li^+ [26,28]. This is reinforced by constant current discharge and charge results, where the reduction and oxidation capacity of 115 mAh g^{-1} and 355 mAh g^{-1} was obtained (**Fig. 3a**). These capacities obtained from LPSCl redox, explain the additional charge capacity observed in the sulfur cells, which is also recoverable upon subsequent discharge. Reversible behavior of LPSCl is also observed within the Li_2S voltage window, delivering a high reversible capacity of 400 mAh g^{-1} (**Fig. 3b**). Assuming this behavior is consistent when paired with Li-S cathodes, expected redox products of the LPSCl electrolyte can be predicted. Complete oxidation of LPSCl forms sulfur, LiCl, and P_2S_5 with reduction products being Li_2S, LiCl, and Li_3P.[26,42] In both redox pathways, LPS is formed intermediately. From the experimentally obtained capacities, the expected reaction can be hypothesized where upon discharge and charge, a lithium rich Li_4PS_4 and lithium deficient $Li_{2.5}PS_4$ can be formed.

$$Li_6PS_5Cl + 1\ Li^+/e^- \longrightarrow Li_2S + Li_4PS_4 + LiCl$$
$$Q_{red} / \textit{Capacity} \approx \textit{100 mAh g}^{-1}$$

$$Li_2S + Li_4PS_4 + LiCl \longrightarrow Li_{2.5}PS_4 + S + 3.5\ Li^+/e^-$$
$$Q_{ox} / \textit{Capacity} \approx \textit{350 mAh g}^{-1}$$

$$Li_2S + Li_4PS_4 \leftrightarrow Li_{2.5}PS_4 + S + 3.5\ Li^+/e^-$$
$$Q_{reversible} / \textit{Capacity} \approx \textit{350 mAh g}^{-1}$$

The electrochemical cycling results of LPSCl allow us to isolate sulfur utilization. In this system, stable sulfur utilization above 80% is achieved (**Fig. 3c**). This can be attributed to the enhanced

ionic transport and ionically conductive interfaces formed during synthesis. Additionally, between this cutoff voltage, cyclic voltammetry sweeps of both sulfur and LPSCl composites reveal their coupled reversible behavior (**Fig. 3d**). The upper voltage cutoff below 3.5 V limits the complete oxidation of LPSCl, preserving ionic conductivity with continued cycles. The high oxidative tendency of LPSCl at 2.3 V vs. Li/Li$^+$ can be effective at reducing the activation potential of Li_2S. This was already observed with the Li_2S cathode, where the activation voltage observed in this work is 2.4 V, without requiring the use of catalysts or kinetic promoters.

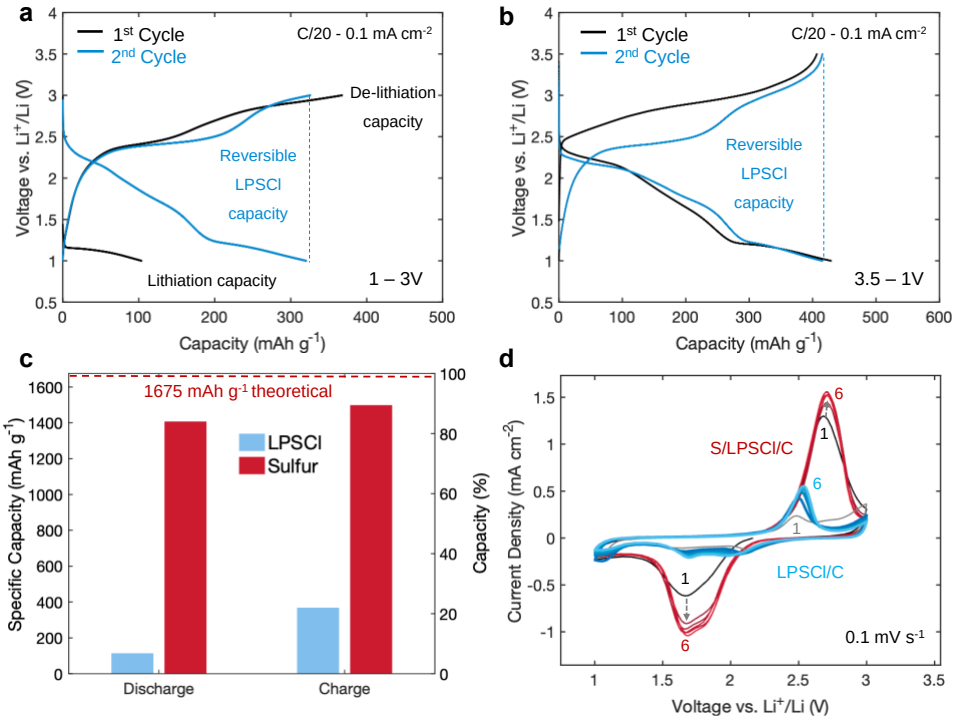

Fig. 3 | Evaluating LPSCl redox activity. Voltage profiles of LPSCl/C composites evaluated under (**a**) sulfur and (**b**) Li_2S voltage limits. **c**, Specific capacity, and capacity contributions of sulfur and LPSCl. **d**, Cyclic voltammetry of S/LPSCl/C and LPSCl/C composites.

To verify the reversibility of the cathode composites, redox products during the 1st formation cycle were investigated. *In-situ* electrochemical impedance spectroscopy (EIS) was performed on the sulfur cathode at each state of charge (**Fig. 4a**). After discharge, impedance growth attributed to the charge transfer resistance from Li_2S formation was observed. After charging, the charge transfer resistance reduces and returns near the pristine state, indicating good reversibility. Post-mortem analysis was conducted to confirm Li_2S formation and conversion, where diffraction peaks attributed to nanocrystalline Li_2S are detected in the XRD spectra after discharge (**Fig. 4b)**, supporting the high utilization of sulfur. After charging, Li_2S is undetectable, indicating its complete oxidation, while the formation of sulfur at 10.5° 2θ is observed. Given the high charge capacity, the low peak intensity and amorphous background suggest that the reformed sulfur is amorphous as in the pristine state. This also suggests the sulfur-SSE conductive interphase is preserved with cycling. TGA results at the discharged and charged states further reinforce high sulfur utilization and the reversibility of this system (**Fig. 4c**).

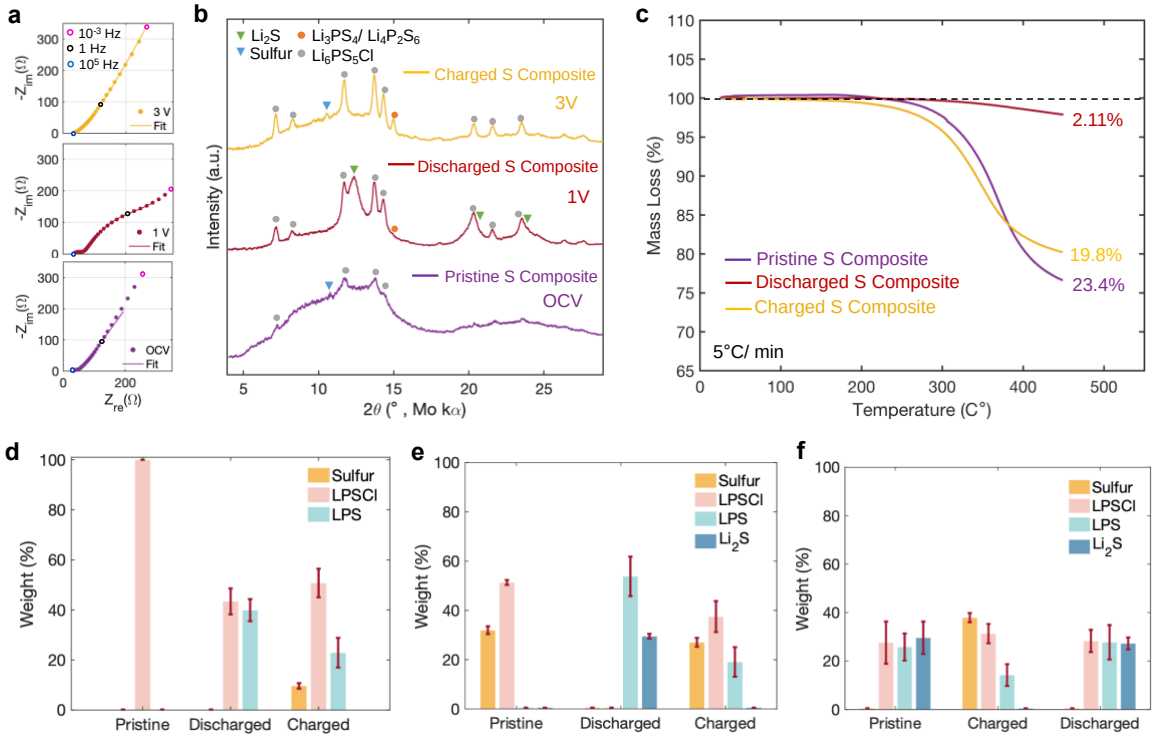

Fig. 4 | Probing electrochemical reversibility. a, Nyquist plots of *in-situ* EIS measurements of the sulfur cathode composite during the first formation cycle. **b**, XRD and (**c**) TGA of the sulfur composite at the pristine, discharged, and charged states. XANES fitting results, representing weight percentages of products at each state of charge for (**d**) LPSCl (**e**) sulfur, and (**f**) Li_2S composites.

However, fully deconvoluting the redox products between LPSCl, sulfur, and Li_2S are challenging. Therefore, XANES spectra at the Sulfur K-edge were measured for all the composites with reference spectra reported in **Fig. S9**. Using the reference spectra, linear combination fit (LCF) analysis can be used to quantify species.[43,44] These fitting spectra are reported in **Fig. S10**, **Fig. S11,** and **Fig. S12**. As hypothesized from the electrochemical results for the LPSCl/C case, 39.9 wt.% of LPS is predicted after discharge, suggesting that half of the LPSCl formed the lithium rich $L_{4.1}PS_4$ phase. After charging, 9.7 wt.% is sulfur with some LPS reforming LPSCl (**Fig. 4d**). These results support the formation of LPS as a redox intermediate, where its reversible redox behavior likely improves the kinetics of Li_2S oxidation. LCF results for the sulfur and Li_2S system also support the reversible electrochemical behavior. For the XANES sulfur fitting results in **Fig. 4e**, 29 wt.% of Li_2S is estimated after the initial discharge, indicating good conversion efficiency. After charging, Li_2S was converted back to sulfur. The additional capacity observed in the formation cycle can be attributed to LPS and a small amount of sulfur from LPSCl oxidation. These results coupled with EIS, XRD, and TGA support the high conversion efficiency attributed to the formation of the ionically conductive interphase layer and the redox activity of the LPSCl electrolyte. Similar conclusions can be drawn for the Li_2S system**.** Complimenting findings revealed by XRD and Raman, half of the LPSCl decomposes to LPS after synthesis (**Fig.4f**). Nevertheless, the amorphous LPS/LPSCl mixture retains its ionic conductivity, supported by the Li_2S electrochemical performance and XANES results. A complete summary of the fitting results can be found in table *S2*.

Enhancing rate and cycling stability. The previous electrochemical performances were obtained using unmodified bulk sulfur and Li_2S, where particle sizes were on the order of 100 microns for sulfur (**fig. S13a**) and 30 microns for Li_2S (**fig. S14**). These sizes, while sufficient for low cycling rates, need to be reduced to improve Li^+ transport and enable higher rate operation. Sulfur particle sizes were produced on the micron and sub-micron scale (**fig. S13**). Given the many possible compositions, geometrical modeling was conducted to aid in experimental design, connecting particle size and composition to active surface areas and transport properties. Sulfur cathode geometries were stochastically generated, with the sulfur as spherical particles and the carbon additives as aggregates (**Fig. 5a**). To compare with experimental capabilities, particle size ranges for bulk, micron, and sub-micron sulfur was 25 to 50 µm, 0.5 to 5 µm, and 0.25 to 0.5 µm, respectively. **Figure 5b** shows the evolution of the active surface area as a function of AM content. The reported values are the average over three repetitions. Intuitively, the sub-micron electrode exhibited the highest active surface area for all AM contents (%), followed by the micron sulfur, and bulk sulfur electrode. Therefore, sub-micron sulfur particles are expected to achieve the highest utilization due to more SSE contact. The tortuosity of the LPSCl phase was explored with the reported value being the average tortuosity in all directions. Surprisingly, the micron sulfur electrode exhibits the lowest ionic transport tortuosity, with all cases obtaining similar results until higher AM contents (**Fig. 5c**). The geometrical modeling results suggest that sub-micron particles may be the best choice to achieve high utilization, yet high active wt.% may be challenging to implement since the ionic transport tortuosity increases drastically after 50 wt.%. Despite the expected high utilization with sub-micron particles from higher surface areas, it must be noted that the geometrical modeling does not consider the (chemo)mechanical effects from lithiation.

To validate the modeling results, room temperature electrochemical performance was conducted for each particle class in LiIn half cells. All particle sizes deliver comparable discharge capacities during the 1st formation cycle at low rates (0.08 mA cm^{-2}) (**Fig. 5d**). The sub-micron sulfur cell delivers the highest discharge capacity of 1694 mAh g^{-1}, beyond the theoretical. This was followed by micron and bulk sulfur which delivered 1615 mAh g^{-1} and 1500 mAh g^{-1}, respectively. This suggests that more LPSCl redox activity can be activated with higher surface area particles. Higher charge capacities are also observed for all cells, reinforcing the additional capacity from the LPSCl electrolyte. The additional charge capacity results in a higher discharge capacity from the 2nd formation cycle with a reduction in cell polarization from 577 mV to 452 mV (**fig. S15a**). The reduced cell polarization could either be from LPSCl redox products or from potentially beneficial (chemo)mechanical behavior. Rate capability was also conducted up to 1C (1.6 mA cm^{-2}) (**fig. S15b)**. The current density at 1C is beyond the critical current for the LiIn anode (~ 1 mA cm^{-2})[45], however, all three cells deliver reasonable utilization at all rates, with bulk sulfur delivering the lowest due to kinetic limitations. Since LPSCl was found to contribute capacity, the specific capacity considering both sulfur and LPSCl masses show reasonable utilization (700 mAh g^{-1}) for both micron and sub-micron at these rates. This is critical for solid-state, as the catholyte is usually considered inactive, responsible for "dead weight" within the cell. In this work, the catholyte contributes electrochemically to the overall cell capacity.

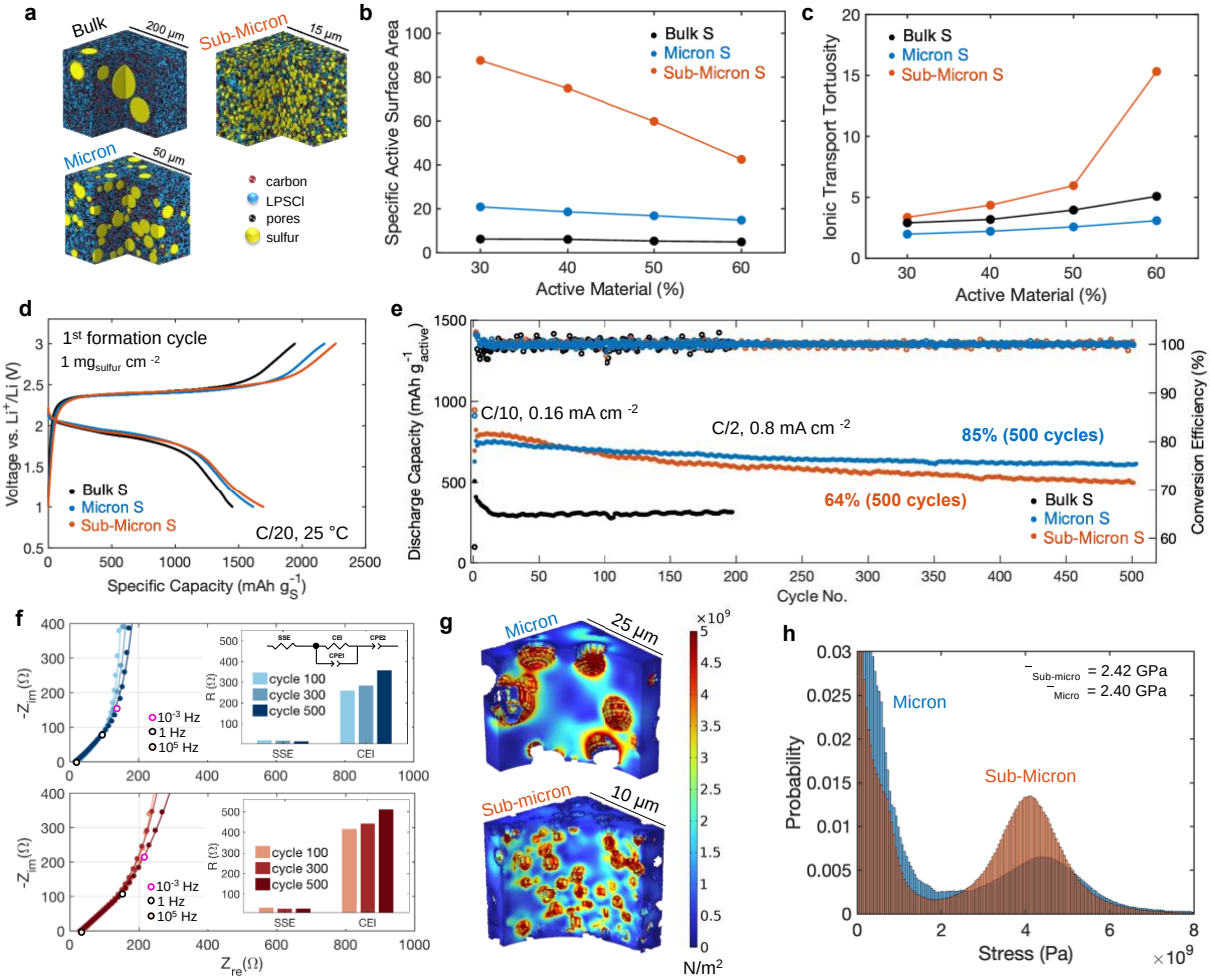

Fig. 5 | Modeling sulfur cathode microstructures with electrochemical validation. a, Geometrically modeled sulfur composite electrodes for bulk, micron, and sub-micron sulfur particles. **b**, Specific active surface area and (**c**) ionic transport tortuosity as a function of AM content (%) and particle size. **d**, First formation cycle voltage profiles of sulfur composites with bulk, micron, and sub-micron particles at C/20. **e**, Long-term cycling stability at C/2 with discharge capacity being normalized by the active mass (sulfur and LPSCl). **f**, Nyquist plots and equivalent circuit fitting results from EIS measurements of the micron (top) and sub-micron (bottom) cathodes at cycle 100, 300, and 500. **g**, Distribution of the von Mises stress on the SSE matrix after simulated lithiation. **h**, Predicted variation of maximum von Mises stress.

Longer term higher rate cycling was evaluated to investigate the particle size effect on cycle life (**Fig. 5e**). The bulk sulfur composite exhibits fast decay, due to longer Li^+ transport lengths from large sulfur particles and poor contact observed after densification (**fig. S13g)**. Despite achieving the highest utilization, the sub-micron sulfur composite delivers 64% retention, with micron being the most stable system, achieving 85% retention after 500 cycles. The retention of the sub-micron cells is significant for Li-S in ASSB at room temperature. Nevertheless, a 20% increase in retention with micron scale particles is a large improvement. The capacity fade of sub-micron cells may be due to excessive decomposition from higher surface area between the carbon and SSE. To test this, cells were constructed with the micron sulfur composite using carbons that possess different specific surface areas and morphologies (**fig. S16**), each chosen to intentionally

facilitate more SSE redox activity. Increasing the carbon surface area increased utilization, mainly from the SSE, but showed no impact on cycling stability. This means the decay observed with the sub-micron sulfur composite is likely of (chemo)mechanical origin, causing degradation at sulfur/SSE particle interfaces. This interfacial degradation should result in impedance growth, where EIS was measured after 100, 300, and 500 cycles (**Fig. 5f**). The intermediate frequency range was assigned to the cathode electrolyte interphase (CEI).[46] The sub-micron sulfur cells do possess higher resistance after 100 cycles, attributed to more mechanical degradation with continued cycling. However, these results differ slightly. Cross-section scanning electron microscopy (SEM) imaging may be useful, although both composites were found to show indistinguishable morphology (**fig. S17**). Therefore, mechanical-based simulations using the generated electrodes in **Fig. 5a** may shed insight on the accumulated stresses at these interfaces.

Sulfur cathodes undergo large volume expansion upon lithiation[47] resulting in internal stresses at their interfaces. To simulate this mechanism, volume changes were estimated based on % utilization for each particle size using 1st cycle discharge capacities based on sulfur mass and subtracting the expected capacity from LPSCl (**fig. S18**). Simulations were conducted using finite element method (FEM) where the sulfur particles underwent the prescribed volume expansion derived from the electrochemical results. Parameters and equations used in the simulations can be found in table *S3* and *S4*. **Figure 5g** displays the distribution of maximum von Mises stress on the SSE matrix, where for both micron and sub-micron cases, stresses beyond 5 GPa were predicted. A bimodal stress distribution shown in **Fig. 5h**, highlights most of the SSE matrix does not experience stress since only 30 wt.% of sulfur is used in the simulation. However, at the cathode interface, the sub-micron sulfur composite experiences a higher frequency of stress from more volume expansion and increased tortuosity. Stress accumulated at the boundaries of the sulfur particles can propagate when these particles are in proximity, creating thinner SSE channels that experience much higher stress versus the bulk. If SSE fracture occurs, pore formation is possible after (de)lithiation. These simulations only capture stress after the 1st lithiation. However, SSE degradation is expected to accumulate with cycling, disrupting ion conduction pathways and leading to more capacity fade as observed in **Fig. 5e**. Electrochemical evaluation, coupled with FEM simulations uncover that sub-micron sulfur particles create a microstructure with high electrode tortuosity, resulting in higher interfacial stresses and faster capacity decay. Previous studies have required nano-scale particles to achieve reasonable utilization[48–50]. However, in this work, micron-scale particles can deliver both high active surface area and low electrode tortuosity, balancing both high utilization and stable cycling, critical for practical Li-S cathodes.

Morphological evolution of Li-S cathodes. In ASSBs, Li-S cathodes are expected to experience (chemo)mechanical degradation from their large volume changes. This will result in stresses on various interfaces as simulated above. Electrochemical performances of sulfur, Li_2S, and LPSCl were found to be highly reversible, but this impact on cathode morphology remains unknown. To visualize this, cross-sectional SEM images were prepared for both micron sulfur and Li_2S cells at each state of charge. Both pristine sulfur and Li_2S cathodes exhibit a dense composite structure, possessing a thickness of 26 µm and 45 µm, respectively, and good interfacial contact (**Fig. 6a and 6b**). Calculations were done to estimate the volume change (%) as a function of sulfur cathode wt.% assuming complete lithiation (**fig. S19**). Here, 25.8 vol.% change is expected, resulting in a thickness increase to 32.7 µm, close to the observed result. The lithiation capacity of this cell was 1.22 mAh. Therefore, the thickness increase of the cathode equates to 4.9 µm mAh^{-1}, which is the expected thickness growth of Li metal with cycling[51]. This suggests that lithiating the sulfur

cathode can compensate the volume reduction of stripping Li metal. After completing the 1st cycle, the sulfur cathode thickness was retained but can be resolved by an increase in porosity. These results reveal that during lithiation, the resulting stress on the SSE matrix causes it to plastically deform to accommodate particle expansion. The deformed structure preserves intimate contact to the separator layer and assists structurally during cycling. These findings can also explain the reduction in polarization after the 1st cycle, where subsequent volume expansion is likely supported by the pre-deformed SSE structure. The plastic deformation of the SSE matrix is not surprising, as the simulated stresses estimated above is near the shear modulus of LPSCl[52].

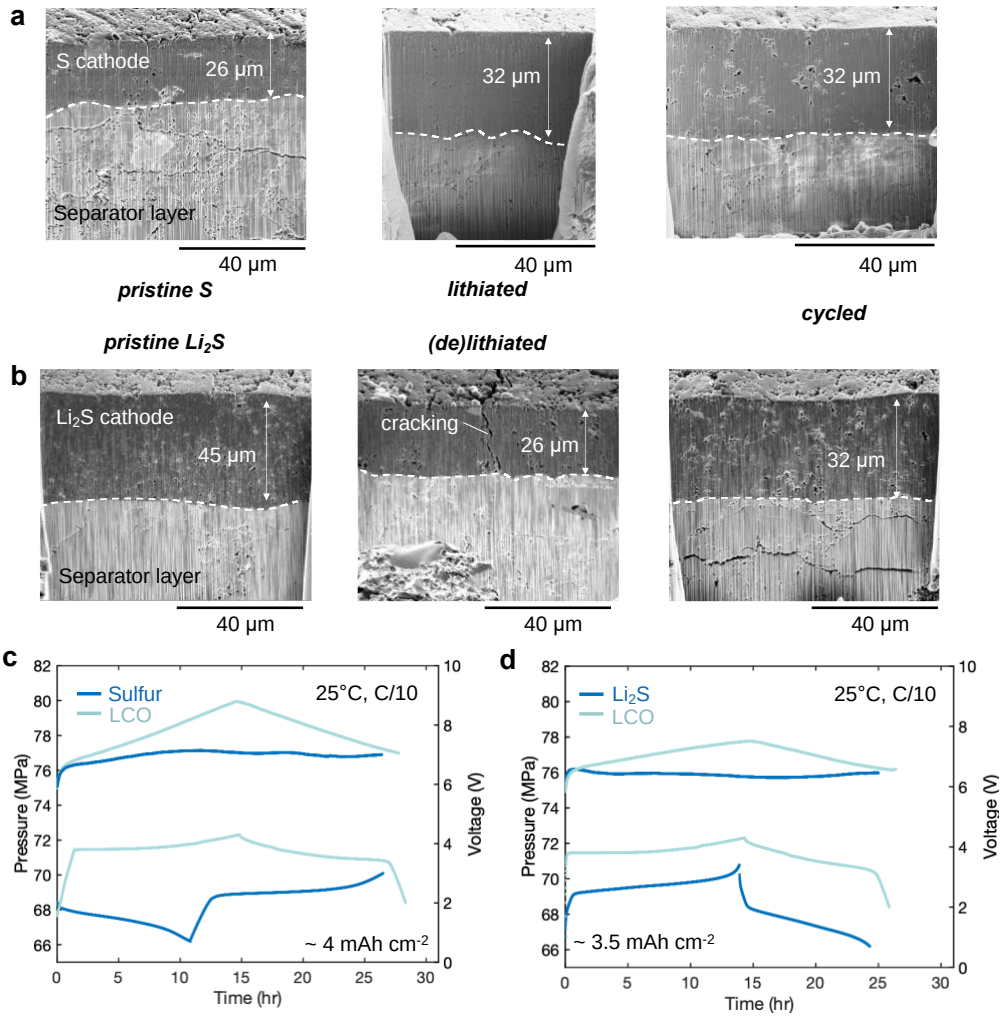

Fig. 6 | Quantifying cathode and cell level volume changes. Cryo-FIB images of the (**a**) micron sulfur and (**b**) Li_2S cathode composite at various states of charge. **c**, *Operando* pressure monitoring of LCO and Sulfur using a lithiated silicon anode and of (**d**) LCO and Li_2S using a µSi anode during the first formation cycle.

The Li_2S cathode is expected to shrink after (de)lithiation. Shown in **Figure 6b**, the Li_2S cathode thickness decreases drastically (~ 40%), where columnar cracking is observed in the cross-section as well as on the surface (**fig. S20**). This cracking is likely strain induced from lithium removal. This morphological phenomenon has been observed in ASSBs using silicon anodes [53] and these results suggest that this (chemo)mechanical behavior is ubiquitous in composite

conversion electrodes when constrained to 2D interfaces. After completing one cycle, the cathode morphology is however, reversible, returning close to the pristine state and is a similar thickness as the electrochemically formed Li_2S in **Fig. 6a**. These results provide two key insights. First, conversion cathodes can alleviate anode volume changes. Second, Li_2S cathodes inherently face more mechanical challenges compared to sulfur due to strain induced cracking after (de)lithiation.

To demonstrate the pressure alleviation proof of concept, *operando* pressure monitoring was conducted comparing $LiCoO_2$ (LCO), sulfur, and Li_2S when paired with µSi and lithiated Si anodes. LCO will expand due to Jahn-Teller distortions[54], although volume expansion is 10 times less than Li-S cathodes. Si is expected to undergo large volume expansion upon lithiation but will be lower than expected due to the constrained 2D interface[53]. Nevertheless, pressure imbalance and resulting (chemo)mechanical degradation is one of the most challenging aspects for solid-state silicon anodes.[55] In theory, using conversion cathodes can relieve internal stresses caused by cycling and to achieve high energy density, high capacity cathodes should be paired with high capacity anodes. Since a lithium source is required for sulfur, cells were assembled using the lithiated silicon anode, where minimal pressure changes with sulfur were observed (**Fig. 6c**). However, the LCO cell pressure increases five times that observed for the sulfur case, with pressure fluctuations consistent with previous studies[56]. When using the µSi anode with Li_2S, almost zero pressure variation is detected during the 1st formation cycle (**Fig. 6d**). The LCO cathode, however, increases by 3 MPa during the charge. Pressure changes from high-capacity anodes can be successfully compensated using conversion cathodes that are highly utilized. This improves cycle life and mitigates cell 'breathing' during cycling, an important consideration for higher loading cells and when integrating cells into pack level architecture.

High loading electrochemical evaluation. High loading cathodes are necessary to achieve high energy density. Therefore, cells with increasing sulfur loadings were constructed and first paired with the LiIn alloy (**Fig. 7a**). Areal capacities up to 11 mAh cm $^{-2}$ with a discharge capacity of 1314 mAh g^{-1} was obtained (**Fig. 7b**), although with a slight increase in polarization, attributed to the high sulfur loading of 7 mg cm $^{-2}$ evaluated at room temperature. Due to the limited critical current density of LiIn alloys, cycling performance of this high loading system was evaluated at 0.52 mA cm $^{-2}$ (**Fig. 7c**), showing minimal decay, with 86.8% retention after 140 cycles. The ability to achieve stable cycling at 11 mAh cm $^{-2}$ at room temperature, demonstrates the effectiveness of the cathode microstructure. To overcome the low current density of LiIn, free standing cathode films were fabricated via dry process method and paired with a Li_2Si anode (**Fig. 7d**). These cells were found to deliver reasonable capacities up to 1C (5.5 mA cm $^{-2}$) as shown in **Fig. 7e**, with full recovery at C/20 (0.3 mA cm $^{-2}$). This dry process sulfur Li_2Si system also demonstrates stable cycling performance at 7.4 mAh cm $^{-2}$, resulting in 77.4% retention after 150 cycles at 1.5 mAh cm^{-2} current densities (**Fig. 7f**).

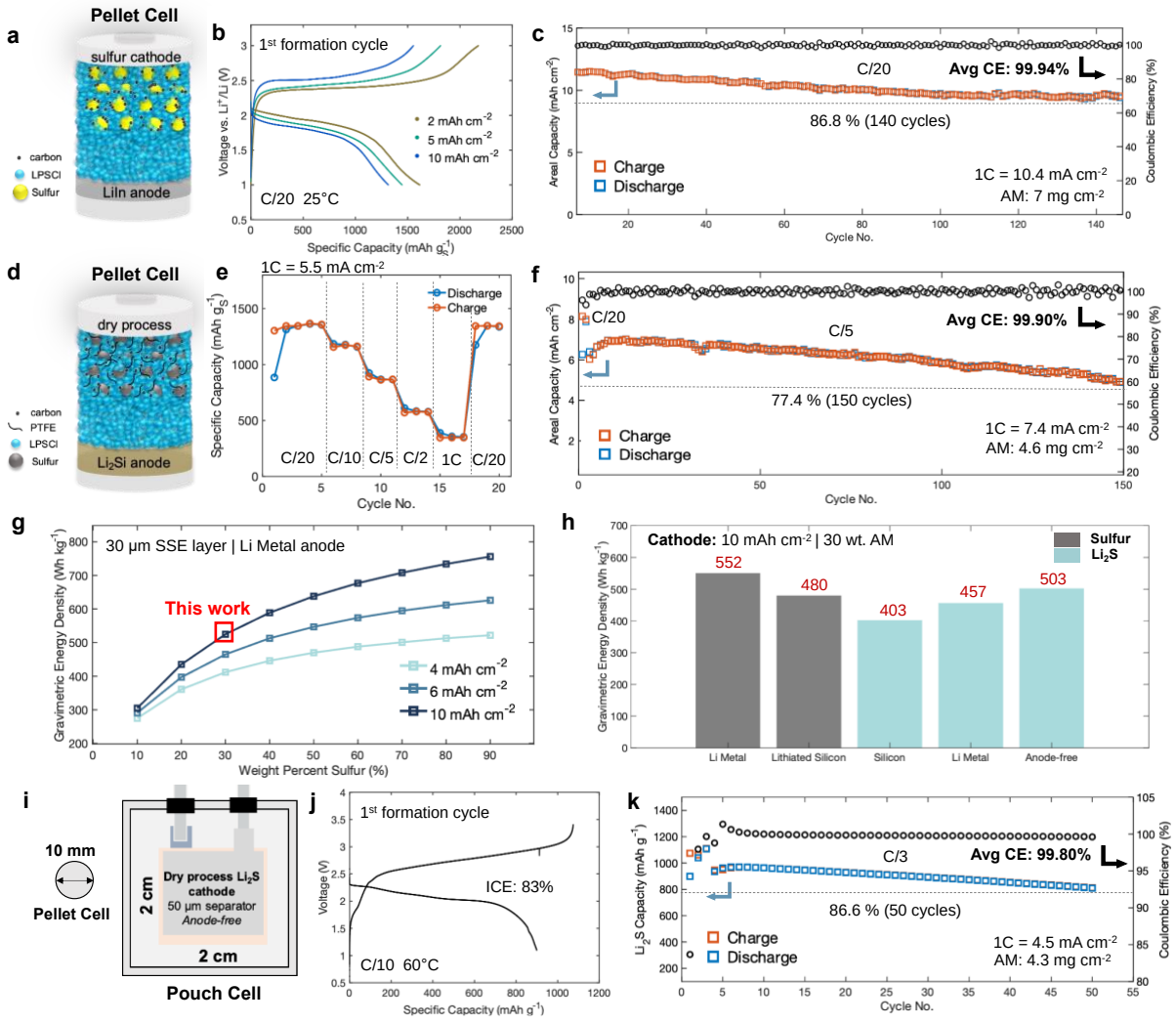

Fig. 7 | Sulfur and Li_2S electrochemical performance with energy density outlook. a, Schematic of the sulfur cathode half-cell architecture in pellet cells. **b**, First cycle voltage profiles with increasing areal capacity. **b**, Long term cycling stability at the 11 mAh cm^{-2} level evaluated at room temperature. **d**, Schematic of the dry process sulfur cathode paired with lithiated silicon in pellet cells. **e**, Rate performance at the 5.5 mAh cm^{-2} level. **f**, Cycling stability at the 7.4 mAh cm^{-2} level under C/5 current density. **g**, Theoretical gravimetric energy density as a function of wt.% of sulfur and areal capacity. **h**, Gravimetric energy density comparison between sulfur and Li_2S cathodes with various anodes. Values used for these calculations can be found in table *S5*. **i**, Schematic of the Li_2S/anode-free pouch cell. **j**, First formation cycle at C/10. **k,** Cycling performance at the 4.5 mAh cm^{-2} level under 10MPa and 60°C conditions.

Pouch cell form factors utilizing thick dry process cathodes, thin separator layers, and high-capacity anodes are necessary to achieve high gravimetric energy densities in all-solid-state.[57] In addition, high areal capacity and active weight percentages are also required. Illustrated in **Fig. 7g**, even lower weight percentages of sulfur at 10 mAh cm $^{-2}$ can realize 500 Wh kg $^{-1}$ and is likely a more promising approach than increasing the weight percentage of sulfur. This is because after lithiation, the volume of SSE compared to lithiated sulfur will reduce. Despite sulfur possessing a

higher specific capacity than its Li_2S counterpart, anode selection is limited to those with a lithium source, making lithium metal or pre-lithiated silicon the only practical option, regardless of their high costs and manufacturing challenges. Using the cathode composition reported in this work, Li_2S can achieve over 400 Wh kg^{-1} using silicon as the anode and go beyond 500 Wh kg^{-1} if combined with an anode-free architecture (**Fig. 7h**). Therefore, a 15 mAh pouch cell was constructed without an anode, utilizing dry process methods, and reducing the separator layer thickness from 500 µm to 50 µm (**Fig. 7i)**. Industry standard formation rates and cycling protocols were used, where this configuration delivers high utilization (1077 mAh g^{-1}) and ICE of 83% (**Fig. 7j)**. Stable cycling at C/3 (1.5 mA cm^{-2}) was also achieved at relatively low stack pressures compared to the pellet-type cells (**Fig. 7k)**.

The electrochemical performances above showcase the versatility of the cathode design methodology, where appropriate synthesis, SSE selection, and optimal cathode microstructure are critical for Li-S chemistry to achieve high utilization and stable cycling. Overall, this approach solves the interfacial, kinetic, and (chemo)mechanical challenges associated with Li-S cathodes in ASSBs. Our work provides a thorough electrochemical, mechanical, and morphological analysis of the critical features required to enable high loading and practical Li-S cathodes. The successful implementation with Li_2Si, µSi, and anode-free architectures presents a promising pathway towards advancing the development of safe and low-cost next-generation high energy density batteries.

Methods

Materials preparation and composite fabrication. Materials were dried under vacuum at 80ºC if not anhydrous and stored and prepared in an argon-filled glovebox. The solid-state electrolyte separator layer and catholyte used is LPSCl for its high conductivity (3 mS cm^{-1} at room temperature) purchased from NEI Corporation. When used as a catholyte, LPSCl was milled at 400 rpm for 2 hours to reduce its particle size to near 10 microns using a high energy planetary ball mill. For the sulfur cathode, elemental sulfur (99.98%, Sigma Aldrich) was either used as received or milled at 400 rpm for 10 and 24 hours for micron and sub-micron particles. For the Li_2S cathode, Li_2S was either used as received (99.98%, Sigma Aldrich) or milled following similar procedures as sulfur. For electrochemical evaluation, optimal cathode composites were milled for 1 hour (unless otherwise specified) at 500 rpm using a planetary ball mill. Other composite trials were either first milled with carbon and sulfur at 500 rpm for 1 hour, followed by hand mixing the SSE or hand mixing all components for 1 hour. The composites consisted of 30 wt.% cathode active material, 50 wt.% LPSCl and 20 wt.% of a conductive agent (acetylene black, vapor grown carbon fiber, or Ketjen black (EC-600JD)).

Dry process cathode fabrication. Cathode composite powders were mixed with 1 wt.% PTFE (Chemours) in a hot mortar and pestle until dough like consistency is formed. The cathode composite was then hot rolled (MTI corp.) under 60°C conditions with decreasing thickness until a 300 to 200-micron film was made.

SSE film and anode-free layer fabrication. For the SSE film preparation, LPSCl (98 wt.%) and an acrylate binder (2 wt.%) were mixed in p-xylene (Sigma Aldrich). The resulting mixture was casted on a polyethylene terephthalate film and dried under vacuum at 40°C overnight. The slurry for anode-free layer was prepared by mixing carbon black (Imerys), silver nanoparticles, and polyvinylidene fluoride (Solvay) in N-methylpyrrolidone (Sigma Aldrich) at a weight ratio of

69.75:23.25:7.0 as described by Lee et al.[58] This slurry was coated onto a 10 μm thick stainless-steel foil using a doctor blade and subsequently dried in a vacuum oven at 100°C overnight.

Electrochemical Measurements. Electrochemical measurements were performed in custom 10 mm diameter pellet cells constructed out of Grade 5 titanium plungers and polyether ether ketone (PEEK) dies. For cell evaluation and CV measurements, the cathode and separator layers are pressed to 3 tons (375 MPa), while the Li_1In or Li metal anode is pressed to 1 ton (125 MPa) or 0.2 ton (25 MPa), respectively. After assembly, the pellet cells are inserted into custom cell holders and hand tightened to 75 MPa unless otherwise stated. EIS, CV, and LSV measurements were collected using a Biologic SP-300 potentiostat. For EIS measurements, an applied voltage amplitude of 30mV and frequency range of 7 MHz to 20 mHz was used. For LSV and CV measurements, a sweeping rate of 0.1 mV/s was used with voltage ranges between the operating voltage of sulfur (1-3V vs. Li/Li^+). For all electrochemical performance evaluation, elemental sulfur cells were cycled under 75 MPa (unless otherwise stated) at room temperature with either Li_1In_1 or Li_2Si acting as the counter electrode. The method to prepare the Li_2Si anode followed protocols outlined in prior work[59]. Li_2S cells were cycled at room temperature with casted Si anodes as described in previous work[53]. Capacity utilization and cell cycling was evaluated using Neware Instrument cyclers (CT-4008T).

Pouch cell fabrication. Al foil, dry processed Li_2S cathode, SSE film and anode, were stacked, and packed into a pouch. The pouch was vacuum-sealed and pressed to 500 MPa at 80°C using warm isostatic pressure (WIP).

Scanning electron microscopy. Scanning electron microscopy (SEM) was performed on a FEI Apreo and/or FEI Scios DualBeam focused ion beam (FIB)/SEM with 5 kV accelerating voltage and 0.1 nA beam current for powders and pellets. Powder and pellet samples were prepared in an argon-filled glovebox and transferred using the air-tight transfer arm to avoid any air exposure. For FIB cross-sectional images, milling was done under cryogenic conditions (-180°C) where Ga was used as an ion beam source. Parameters used for all milling conditions of 30 kV, 65 nA, with the subsequent cross-section cleaning performed with 30 kV, 15 to 7 nA, if necessary.

X-ray Diffraction. XRD measurements were collected over a 5 – 50° 2θ range on a Bruker ApexII-Ultra CCD microfocus Rotating Anode instrument with Mo K_α (λ = 0.7107 Å) radiation at the UCSD X-Ray Crystallography Department. Samples were prepared in an argon-filled glovebox using 0.7 mm boron capillaries, and flame sealed to ensure air-tight measurements of sensitive samples.

X-ray Photoelectron Spectroscopy. XPS measurements were conducted using a Kratos Axis Supra XPS instrument. Al Kα radiation was used, with a chamber pressure of less than 5×10^{-8} torr during operation. A charge neutralizer was used for insulating samples and the scan resolution was 0.1 eV with a dwell time of 100 ms. CasaXPS was used for fitting and analysis.[60] The data was calibrated based on the C 1s peak at 285 eV where a Shirley-type background was used.

Transmission electron microscopy. The sample was mounted to an airtight cooling holder from Melbuild to eliminate any contaminations to the sulfur/LPSCl/C samples and transferred to the TEM column directly without any air or moisture exposure. The sample was cooled down to cryogenic conditions (~180°C) and stabilized for additional 30 minutes before electron beam

exposure. (S)TEM results were obtained on ThermoFisher Talos X200 equipped with a Ceta camera operated at 200 kV with low dose capability. The energy dispersive X-ray spectroscopy (EDS) characterization is installed with compositional mapping using 4 in-column SDD Super-X windowless detectors. The data acquisition was operated at low dose condition to minimize any beam damage to the sample.

X-ray Absorption Spectroscopy. Tender X-ray absorption spectroscopy (XAS) measurements were conducted at Taiwan Light Source (TLS) beamline 16A1 of the National Synchrotron Radiation Research Center (NSRRC) in Hsinchu, Taiwan. The beamline uses a double-crystal Si (111) monochromator for the photon energy range from 2 to 8 keV. All samples were sealed in a pouch made of 2.5 um thick Mylar® film inside an Ar-filled glovebox to prevent the samples from exposure to air. Each sample was mounted onto the holder and placed in the measuring chamber at an angle of 45° to the incident X-ray beam. The chamber is constantly purged with He to reduce the X-ray attenuation for at least 45 minutes before collecting the XAS data. The Sulfur *K*-edge X-ray absorption near-edge structure (XANES) spectra were collected in the total fluorescence yield (TFY) mode using a Lytle detector with a scanning step of 0.2 eV. The photon energy was calibrated to 2472 eV (maximum in the 1st derivative) at the S *K*-edge using elemental sulfur. The XANES spectra background subtraction, normalization, and the Linear Combination Fit (LCF) were performed on Athena software. [61]

Modeling of sulfur electrode geometries. The electrodes structures were stochastically generated using the MATLAB codes from Duquesnoy et al.[62], with the S as spherical particles, and the carbon additives as aggregates. A volume fraction of 10% was dedicated to pores, the S amount ranged from 30 to 60%, and the volume ratio between the LPSCl and carbon additives was kept constant at 5:2. Three different cases were investigated, Bulk, Micro and Nano, with S radii ranging respectively from 25 to 50 µm, 0.5 to 5 µm, and 0.25 to 0.5 µm. To have a representative volume for each condition, the length of the cubic electrodes was 200 µm for the Bulk, 50 µm for the Micro, and 15 µm for the Nano. For each set of S size and amount, 3 electrodes were generated to obtain statistically relevant observables. The evolution of the active surface area was monitored as the specific surface area, i.e. the ratio between the number of pixels of S in contact with LPSCl and the total number of S pixels. The tortuosity of the LPSCl phase was investigated using TauFactor[63] in MATLAB, and the reported value is the average value of the tortuosity of the electrolyte phase in all directions.

Finite Elements Method (FEM) Simulations. The electrodes were meshed using the open-access toolbox Iso2Mesh[64] and later imported into COMSOL Multiphysics 6.1. There, using the Solids Mechanics module, the set of parameters and equations in Table S3 and Table S4 were set. In the model, the electrode was assumed to be fully compact (no porosity) and the S particles were uniformly lithiated throughout the simulation, leading to a volume expansion made possible with the "Hygroscopic Swelling" node which normally accounts for the volume expansion of solids due to the amount of water. During the simulation, the external boundaries of the electrode were fixed. To determine the analog hygroscopic coefficient of each type of S particles, a 2-D simulation consisting of the exact same model for a single S particle was performed. The hygroscopic coefficient was deemed adequate when the S particle would reach the desired volumetric expansion (controlled here by its radius) at full lithiation. The cases of sub-micro and micron S were investigated through FEM simulations for an AM content of 30 wt.% where three electrodes were used for each case, and the value reported in the manuscript are averaged over all three electrodes.

Acknowledgments

The authors would like to acknowledge the UCSD Crystallography Facility. This work was also performed in part at the San Diego Nanotechnology Infrastructure (SDNI) of UCSD, a member of the National Nanotechnology Coordinated Infrastructure, which is supported by the National Science Foundation (Grant ECCS-1542148), along with the use of facilities and instrumentation supported by NSF through the UC San Diego Materials Research Science and Engineering Center (UCSD MRSEC), grant #DMR-201192. The authors would like to also acknowledge the use of facilities and instrumentation at the UC Irvine Materials Research Institute (IMRI), which is supported in part by the National Science Foundation through the UC Irvine Materials Research Science and Engineering Center (DMR-2011967). The XPS work was performed using instrumentation funded in part by the National Science Foundation Major Research Instrumentation Program under grant No. CHE-1338173. **Funding:** This work was funded by the LG Energy Solution through the Frontier Research Laboratory (FRL) Program. A.C. acknowledges the National Science Foundation for having supported their Ph.D. research through the NSF Graduate Research Fellowship Program.

Author contributions. A.C. and Y.S.M. conceived the ideas for the study. A.C., J.B.L., and X.W. designed the experiments. B.S., P.R., G.D., C.H., D.C., and A.C. performed the XRD, XPS, XAS, FIB, and TGA experiments. M.C. performed the modeling and FEM simulations. C.L. and D.L. fabricated and evaluated the pouch cells. J.A.S.O., G.D., S.-Y.H., H.Y., M.V., J.J., M.-S.S., J.B.L., and Y.S.M. participated in the scientific discussion and data analysis. A.C. wrote the manuscript. All authors discussed the results and commented on the manuscript. All authors have approved the final manuscript.

Competing interests. Two patents were filed for this work through UC San Diego's Office of Innovation and Commercialization and LG Energy Solution, Ltd.

References

1. A. Marjolin. Lithium-ion battery capacity to grow steadily to 2030. *S&P Global Market Intelligence* (2023).

2. B. A. Adu-Gyamfi, C. Good, Electric aviation: A review of concepts and enabling technologies. *Transportation Engineering*, **9**, 100134, (2022).

3. D. A. Dornbusch, R. P. Viggiano, J. W. Connell, Y. Lin, V. F. Lvovich, Practical considerations in designing solid state Li-S cells for electric aviation. *Electrochim Acta*, **403** (2022).

4. A. Manthiram, Y. Fu, Y. S. Su, Challenges and prospects of lithium-sulfur batteries. *Acc Chem Res* **46**, 1125–1134 (2013).

5. J. Sun, T. Wang, Y. Gao, Z. Pan, R. Hu, J. Wang, Will lithium-sulfur batteries be the next beyond-lithium-ion batteries and even much better? *InfoMat*, DOI: 10.1002/inf2.12359 (2022).

6. J. R. Akridge, Y. V. Mikhaylik, N. White, Li/S fundamental chemistry and application to high-performance rechargeable batteries. *Solid State Ionics*, **175**, 243-245 (2004).

7. Ren, W., Ma, W., Zhang, S. Tang, B. Recent advances in shuttle effect inhibition for lithium sulfur batteries. *Energy Storage Materials*, **23,** 707–732 (2019).

8. S. Ohno, W. G. Zeier. Toward Practical Solid-State Lithium-Sulfur Batteries: Challenges and Perspectives. *Acc Mater Res.,* **2**, 869–880 (2021).

9. A. Manthiram, Y. Fu, S. H. Chung, S. Zu, Y.S. Su. Rechargeable lithium-sulfur batteries. *Chemical Reviews* vol. 114 11751–11787, (2014).

10. J.A., Lewis, J. Tippens, F. J. Q., Cortes, M.T., McDowell. Chemo-Mechanical Challenges in Solid-State Batteries. *Trends in Chemistry* vol. 1 845–857 (2019).

11. M. Chen, S. Adams, High performance all-solid-state lithium/sulfur batteries using lithium argyrodite electrolyte. *Journal of Solid-State Electrochemistry*, **19**, 697–702 (2015).

12. S. Kinoshita, K. Okuda, N. Machida, M. Naito, T. Sigematsu, All-solid-state lithium battery with sulfur/carbon composites as positive electrode materials. *Solid State Ion.,* **256**, 97–102 (2014).

13. C. Yu, L. van Eijck, S. Ganapathy, M. Wagemaker, Synthesis, structure, and electrochemical performance of the argyrodite Li_6PS_5Cl solid electrolyte for Li-ion solid state batteries. *Electrochim Acta*., **215**, 93–99 (2016).

14. X. Zhu, W. Jiang, S. Zhao, R. Huang, M. Ling, C. Liang, L. Wang, Exploring the concordant solid-state electrolytes for all-solid-state lithium-sulfur batteries. *Nano Energy*, **96** (2022).

15. H. Kim, H. N. Choi, J. Y. Hwang, C. S. Yoon, Y. K. Sun, Tailoring the Interface between Sulfur and Sulfide Solid Electrolyte for High-Areal-Capacity All-Solid-State Lithium-Sulfur Batteries. *ACS Energy Lett*., 3971–3979 (2023).

16. S. Wang, Y. Zhang, X. Zhang, T. Liu, Y. H. Lin, Y. Shen, L. Li, C. W. Nan, High-Conductivity Argyrodite Li_6PS_5Cl Solid Electrolytes Prepared via Optimized Sintering Processes for All-Solid-State Lithium-Sulfur Batteries. *ACS Appl Mater Interfaces*, **10**, 42279–42285 (2018).

17. Y. Zhang, T. Liu, Q. Zhang, X. Zhang, S. Wang, X. Wang, L. Li, L. Z. Fan, C. W. Nan, Y. Shen, High-performance all-solid-state lithium-sulfur batteries with sulfur/carbon nano-hybrids in a composite cathode. *J Mater Chem A Mater*, **6**, 23345–23356 (2018).

18. X. Yao, N. Huang, F. Han, Q. Zhang, H. Wan, J. P. Mwizerwa, C. Wang, X. Xu, High-Performance All-Solid-State Lithium–Sulfur Batteries Enabled by Amorphous Sulfur-Coated Reduced Graphene Oxide Cathodes. *Adv. Energy Mater*, **7** (2017).

19. A. S. Alzahrani, M. Otaki, D. Wang, Y. Gao, T. S. Arthur, S. Liu, D. Wang, Confining Sulfur in Porous Carbon by Vapor Deposition to Achieve High-Performance Cathode for All-Solid-State Lithium-Sulfur Batteries. *ACS Energy Lett*., **6**, 413–418 (2021).

20. J. Zhou, M. L. Holekevi Chandrappa, S. Tan, S. Wang, C. Wu, H. Nguyen, C. Wang, H. Liu, S. Yu, Q. R. S. Miller, G. Hyun, J. Holoubek, J. Hong, Y. Xiao, C. Soulen, Z. Fan, E. E. Fullerton, C. J. Brooks, C. Wang, R. J. Clément, Y. Yao, E. Hu, S. P. Ong, P. Liu, Healable and conductive sulfur iodide for solid-state Li–S batteries. *Nature* **627**, 301–305 (2024).

21. K. Fu, Y. Gong, G. T. Hitz, D. W. McOwen, Y. Li, S. Xu, Y. Wen, L. Zhang, C. Wang, G. Pastel, J. Dai, B. Liu, H. Xie, Y. Yao, E. D. Wachsman, L. Hu, Three-dimensional bilayer garnet solid electrolyte based high energy density lithium metal-sulfur batteries. *Energy Environ. Sci.,* **10**, 1568–1575 (2017).

22. H. Yang, L. Wang, C. Geng, Y. Zhao, Q. Li, X. Jiang, Z. Tian, M. Wang, C. Jiang, Z. Sun, B. Cui, Y. B. He, W. Chen, W. Lv, Q. H. Yang, Catalytic Solid-State Sulfur Conversion Confined in Micropores toward Superhigh Coulombic Efficiency Lithium-Sulfur Batteries. *Adv Energy Mater*, doi: 10.1002/aenm.202400249 (2024).

23. Y. Liu, X. Meng, Z. Wang, J. Qiu, A Li_2S-based all-solid-state battery with high energy and superior safety. *Sci. Adv*., **8**, eabl8390 (2022).

24. X. Zhu, L. Wang, Z. Bai, J. Lu, T. Wu, Sulfide-Based All-Solid-State Lithium–Sulfur Batteries: Challenges and Perspectives. *Nanomicro. Lett.,* 15 (2023).

25. D. Wang, L. J. Jhang, R. Kou, M. Liao, S. Zheng, H. Jiang, P. Shi, G. X. Li, K. Meng, D. Wang, Realizing high-capacity all-solid-state lithium-sulfur batteries using a low-density inorganic solid-state electrolyte. *Nat Commun*., **14** (2023).

26. D. H. S. Tan, E. A. Wu, H. Nguyen, Z. Chen, M. A. T. Marple, J. M. Doux, X. Wang, H. Yang, A. Banerjee, Y. S. Meng, Elucidating Reversible Electrochemical Redox of Li_6PS_5Cl Solid Electrolyte. *ACS Energy Lett.*, 2418–2427 (2019).

27. J. Jang, Y. T. Chen, G. Deysher, D. Cheng, S. Y. Ham, A. Cronk, P. Ridley, H. Yang, B. Sayahpour, B. Han, W. Li, W. Yao, E. A. Wu, J. M. Doux, L. H. B. Nguyen, J. A. S. Oh, D. H. S. Tan, Y. S. Meng, Enabling a Co-Free, High-Voltage $LiNi_{0.5}Mn_{1.5}O_4$ Cathode in All-Solid-State Batteries with a Halide Electrolyte. *ACS Energy Lett*., 7, 2531–2539 (2022).

28. A. Cronk, Y. T. Chen, G. Deysher, S. Y. Ham, H. Yang, P. Ridley, B. Sayahpour, L. H. B. Nguyen, J. A. S. Oh, J. Jang, D. H. S. Tan, Y. S. Meng, Overcoming the Interfacial Challenges of $LiFePO_4$ in Inorganic All-Solid-State Batteries. *ACS Energy Lett.,* 8, 827–835 (2023).

29. Z. Lin, Z. Liu, W. Fu, N. J. Dudney, C. Liang, Lithium polysulfidophosphates: A family of lithium-conducting sulfur-rich compounds for lithium-sulfur batteries. *Angewandte Chemie - International Edition*, **52**, 7460–7463 (2013).

30. C. Zheng, K. Wang, L. Li, H. Huang, C. Liang, Y. Gan, X. He, W. Zhang, J. Zhang, High-Performance All-Solid-State Lithium–Sulfur Batteries Enabled by Slurry-Coated Li_6PS_5Cl/S/C Composite Electrodes. *Front Energy Res* **8**, (2021).

31. H. Pan. M. Zhang, Z. Cheng, H. Jiang, J. Yang, P. Wang, P. He, H. Zhou, Carbon-Free and Binder-Free Li-Al Alloy Anode Enabling an All-Solid-State Li-S Battery with High Energy and Stability. *Sci. Adv,* 8, 4372 (2022).

32. X. Gao, X. Zheng, Y. Tsao, P. Zhang, X. Xiao, Y. Ye, J. Li, Y. Yang, R. Xu, Z. Bao, Y. Cui, All-Solid-State Lithium-Sulfur Batteries Enhanced by Redox Mediators. *J Am Chem Soc* **143**, 18188–18195 (2021).

33. S. Ohno, R. Koerver, G. Dewald, C. Rosenbach, P. Titscher, D. Steckermeier, A. Kwade, J. Janek, W. G. Zeier, Observation of Chemomechanical Failure and the Influence of Cutoff Potentials in All-Solid-State Li-S Batteries. *Chemistry of Materials*, **31**, 2930–2940 (2019).

34. R. Schlem, C. F. Burmeister, P. Michalowski, S. Ohno, G. F. Dewald, A. Kwade, W. G. Zeier, Energy Storage Materials for Solid-State Batteries: Design by Mechanochemistry. *Adv. Energy Mater*., **11**, 2101022 (2021).

35. J. T. Kim, S. Hu, Y. Zhong, C. Wang, H. Wu, D. Zhao, C. Wang, X. Sun, Y. Li, All-solid-state lithium–sulfur batteries through a reaction engineering lens. *Nature Chemical Engineering* **1**, 400–410 (2024).

36. F. Chen, P. Puente, Y. Zhang, S. Cao, X. Lu, Z. Yi, Q. Shen, J. Li, All-solid-state lithium-sulfur batteries assembled by composite polymer electrolyte and amorphous sulfur/rGO composite cathode. *Solid State Ion* **380**, (2022).

37. L. Lodovico, S. Milad Hosseini, A. Varzi, S. Passerini, Amorphous Lithium Sulfide as Lithium-Sulfur Battery Cathode with Low Activation Barrier. *Energy Technology* **7**, (2019).

38. L. Li, Z. Ma, Y. Li, Accurate determination of optimal sulfur content in mesoporous carbon hosts for high-capacity stable lithium-sulfur batteries. *Carbon*, **197**, 200–208 (2022).

39. A. T. Ward, Raman Spectroscopy of Sulfur, Sulfur-Selenium, and Sulfur-Arsenic Mixtures. *J Phys Chem*., **72**, 4133–4139 (1968).

40. R. Dominko, A. Vizintin, G. Aquilanti, L. Stievano, M. J. Helen, A. R. Munnangi, M. Fichtner, I. Arcon, Polysulfides Formation in Different Electrolytes from the

Perspective of X-ray Absorption Spectroscopy. *J Electrochem. Soc.,* **165**, A5014–A5019 (2018).

41. M. Tachez, J.-P. Malugani, R. Mercier, G. Robert, Ionic Conductivity of and Phase Transition in Lithium Thiophosphate Li_3PS_4. *Solid State Ionics*, **14**, 181-185 (1984).

42. T. K. Schwietert, V. A. Arszelewska, C. Wang, C. Yu, A. Vasileiadis, N. J. J. de Klerk, J. Hageman, T. Hupfer, I. Kerkamm, Y. Xu, E. van der Maas, E. M. Kelder, S. Ganapathy, M. Wagemaker, Clarifying the relationship between redox activity and electrochemical stability in solid electrolytes. *Nat. Mater*., **19**, 428–435 (2020).

43. M. Cuisinier, P. E. Cabelguen, S. Evers, G. He, M. Kolbeck, A. Garsuch, T. Bolin, M. Balasubramanian, L. F. Nazar, Sulfur speciation in Li-S batteries determined by operando X-ray absorption spectroscopy. *Journal of Physical Chemistry Letters*, **4**, 3227–3232 (2013).

44. A. Manceau, K. L. Nagy, Quantitative analysis of sulfur functional groups in natural organic matter by XANES spectroscopy. *Geochim. Cosmochim. Acta*., **99**, 206–223 (2012).

45. A. L. Santhosha, L. Medenbach, J. R. Buchheim, P. Adelhelm, The Indium−Lithium Electrode in Solid-State Lithium-Ion Batteries: Phase Formation, Redox Potentials, and Interface Stability. *Batteries & Supercaps*, **2**, 524–529 (2019).

46. B. A. Mei, O. Munteshari, J. Lau, B. Dunn, L. Pilon, Physical Interpretations of Nyquist Plots for EDLC Electrodes and Devices. *Journal of Physical Chemistry C*, **122**, 194–206 (2018).

47. J. Gu, Z. Liang, J. Shi, Y. Yang, Electrochemo-Mechanical Stresses and Their Measurements in Sulfide-Based All-Solid-State Batteries: A Review. *Adv. Energy Mater.*, **13**, 2203153 (2023).

48. H. Zhong, Y. Su, R. Ma, Y. Luo, H. Lin, J. Gu, Z. Gong, Y. Yang, Nano-Scale Interface Engineering of Sulfur Cathode to Enable High-Performance All-Solid-State Li–S Batteries. *Adv Funct. Mater*., doi: 10.1002/adfm.202315925 (2024).

49. X. Ji, K. T. Lee, L. F. Nazar, A highly ordered nanostructured carbon-sulphur cathode for lithium-sulphur batteries. *Nat. Mater*., **8**, 500–506 (2009).

50. F. Han, J. Yue, X. Fan, T. Gao, C. Luo, Z. Ma, L. Suo, C. Wang, High-performance all-solid-state lithium-sulfur battery enabled by a mixed-conductive Li_2S nanocomposite. *Nano Lett*., **16**, 4521–4527 (2016).

51. A. Schiele, T. Hatsukade, B. B. Berkes, P. Hartmann, T. Brezesinski, J. Janek, High-Throughput in Situ Pressure Analysis of Lithium-Ion Batteries. *Anal. Chem*., **89**, 8122–8128 (2017).

52. Z. Deng, Z. Wang, I.-H. Chu, J. Luo, S. P. Ong, Elastic Properties of Alkali Superionic Conductor Electrolytes from First Principles Calculations. *J. Electrochem. Soc.*, **163**, A67–A74 (2016).

53. D. H. S. Tan, Y.-T. Chen, H. Yang, W. Bao, B. Sreenarayanan, J.-M. Doux, W. Li, B. Lu, S.-Y. Ham, B. Sayahpour, J. Scharf, E. A. Wu, G. Deysher, H. E. Han, J. Hah, H. Jeong, J. B. Lee, Z. Chen, Y. S. Meng, Carbon-free high-loading silicon anodes enabled by sulfide solid electrolytes. *Science* **373**, 1494–1499 (2021).

54. J. N. Reimers, J. R. Dahn, Electrochemical and In Situ X-Ray Diffraction Studies of Lithium Intercalation in Li_xCoO_2. *J. Electrochem. Soc.*, **139**, 2091–2097 (1992).

55. H. Huo, M. Jiang, Y. Bai, S. Ahmed, K. Volz, H. Hartmann, A. Henss, C. V. Singh, D. Raabe, J. Janek, Chemo-mechanical failure mechanisms of the silicon anode in solid-state batteries. *Nat. Mater.*, **23**, 543-551 (2024).

56. R. Koerver, W. Zhang, L. De Biasi, S. Schweidler, A. O. Kondrakov, S. Kolling, T. Brezesinski, P. Hartmann, W. G. Zeier, J. Janek, Chemo-mechanical expansion of lithium electrode materials-on the route to mechanically optimized all-solid-state batteries. *Energy Environ. Sci.,* **11**, 2142–2158 (2018).

57. D. H. S. Tan, Y. S. Meng, J. Jang, Scaling up high-energy-density sulfidic solid-state batteries: A lab-to-pilot perspective. *Joule*, **6,** 1755-1769 (2022).

58. Y. G. Lee, S. Fujiki, C. Jung, N. Suzuki, N. Yashiro, R. Omoda, D. S. Ko, T. Shiratsuchi, T. Sugimoto, S. Ryu, J. H. Ku, T. Watanabe, Y. Park, Y. Aihara, D. Im, I. T. Han, High-energy long-cycling all-solid-state lithium metal batteries enabled by silver–carbon composite anodes. *Nat Energy,* **5**, 299–308 (2020).

59. S. Y. Ham, E. Sebti, A. Cronk, T. Pennebaker, G. Deysher, Y. T. Chen, J. A. S. Oh, J. B. Lee, M. S. Song, P. Ridley, D. H. S. Tan, R. J. Clément, J. Jang, Y. S. Meng, Overcoming low initial coulombic efficiencies of Si anodes through prelithiation in all-solid-state batteries. *Nat. Commun.,* **15** (2024).

60. N. Fairley, V. Fernandez, M. Richard-Plouet, C. Guillot-Deudon, J. Walton, E. Smith, D. Flahaut, M. Greiner, M. Biesinger, S. Tougaard, D. Morgan, J. Baltrusaitis, Systematic and collaborative approach to problem solving using X-ray photoelectron spectroscopy. *Applied Surface Science Advances,* **5** (2021).

61. B. Ravel, M. Newville, ATHENA, ARTEMIS, HEPHAESTUS: Data analysis for X-ray absorption spectroscopy using IFEFFIT. *Journal of Synchrotron Radiation,* **12**, 537–541 (2005).

62. M. Duquesnoy, T. Lombardo, M. Chouchane, E. N. Primo, A. A. Franco, Data-driven assessment of electrode calendering process by combining experimental results, in silico mesostructures generation and machine learning. *J Power Sources,* **480** (2020).

63. S. J. Cooper, A. Bertei, P. R. Shearing, J. A. Kilner, N. P. Brandon, TauFactor: An open-source application for calculating tortuosity factors from tomographic data. *SoftwareX,* **5**, 203–210 (2016).

64. A. P. Tran, S. Yan, Q. Fang, Improving model-based functional near-infrared spectroscopy analysis using mesh-based anatomical and light-transport models. *Neurophotonics,* **7**, 1 (2020).

Supplementary Information is available for this paper.